

Microwave-functionalized natural tannic acid as an anticorrosive UV-curable coating

Original

Microwave-functionalized natural tannic acid as an anticorrosive UV-curable coating / Sesia, R., Pou I Rodríguez, P., Calovi, M., Hakkarainen, M., Rossi, S., Ferraris, S., Spriano, S., Sangermano, M.. - In: POLYMER. - ISSN 0032-3861. - ELETTRONICO. - 315:(2024). [10.1016/j.polymer.2024.127824]

Availability:

This version is available at: 11583/2994488 since: 2024-11-18T07:17:17Z

Publisher:

Elsevier

Published

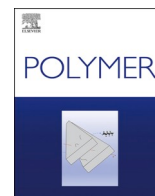
DOI:10.1016/j.polymer.2024.127824

Terms of use:

This article is made available under terms and conditions as specified in the corresponding bibliographic description in the repository

Publisher copyright

(Article begins on next page)



Microwave-functionalized natural tannic acid as an anticorrosive UV-curable coating

Rossella Sesia^a, Paula Pou I Rodríguez^c, Massimo Calovi^b, Minna Hakkarainen^c, Stefano Rossi^b, Sara Ferraris^a, Silvia Spriano^a, Marco Sangermano^{a,*}

^a Department of Applied Science and Technology, Politecnico di Torino, Corso Duca degli Abruzzi 24, 10129, Torino, Italy

^b Department of Industrial Engineering, Università di Trento, Via Sommarive 9, 38123, Trento, Italy

^c Department of Fibre and Polymer Technology, KTH Royal Institute of Technology, Teknikringen 56-58, SE-100 44, Stockholm, Sweden

ARTICLE INFO

Keywords:

Tannic acid
Microwave-assisted methacrylation
Photopolymerization
Anticorrosive coating

ABSTRACT

Corrosion causes serious steel deterioration with consequent negative impacts on the environment and economy. Organic coatings are widely exploited to provide corrosion protection on low-carbon steel. However, the raw materials and preparation methods for common anticorrosive coatings are not sustainable. In this framework, the efficient microwave-assisted methacrylation of a natural polyphenolic compound, tannic acid (TA), provided a UV-curable monomer with a high degree of substitution. The produced methacrylated tannic acid (MTA) was characterized by means of ³¹P NMR and FTIR spectroscopies. The UV-curing of MTA by radical photopolymerization was deeply investigated via the real-time FTIR, photo-DSC, and photo-rheological analyses, confirming the high photo-reactivity of MTA with a conversion of 80 % and a gel point at 2.5 s. The UV-cured MTA showed good thermal stability and a glass transition temperature (T_g) of 133 °C. Furthermore, UV-cured MTA coating exhibited high hardness and hydrophobicity. The zeta potential measurement indicated a negatively charged surface with an isoelectric point (IEP) at pH 2.7. Finally, the good corrosion protection performance of UV-cured MTA coating on plasma pre-treated steel surface was assessed through electrochemical impedance spectroscopy.

1. Introduction

Low alloy steel is the most extensively used structural material in a wide range of areas, including automotive, open-air structures, and industrial pipes, thanks to its affordable price and good mechanical qualities [1,2]. However, the phenomenon of corrosion, to which steel is particularly susceptible, leads to serious drawbacks, such as the loss of productivity, safety concerns, and environmental impacts due to CO₂ emissions associated with steelmaking for the replacement of corroded structures [3,4]. Moreover, the economic impact of corrosion is significant [5]. Thus, numerous strategies are investigated to reduce steel corrosion, from corrosion inhibitors to organic or inorganic coatings [6–8]. The market value of corrosion protection is projected to rapidly grow from \$ 13.5 billion in 2020 to \$ 20 billion by 2027 [9].

Organic protective coatings are a successful and widely used method to prevent corrosion on metallic surfaces in different critical working scenarios. The coating functions as a protective barrier between the steel and the environment providing high resistance to ionic movement [10].

Several types of coatings and application techniques have been proposed in the scientific literature and are industrially used [11–14]. Nevertheless, non-renewable and oil-derived chemicals are commonly exploited in processes of anticorrosive coating production [15], increasing the concern about environmental impacts. Hence, the development of sustainable coatings from renewable sources following the green chemistry principles is an urgent need [16]. Bio-based monomers derived from plants and agro-food waste, especially vegetable oils, have been recommended as potential alternatives [16–23].

Among natural sources, the interest in natural polyphenolic compounds is rising due to their availability, ease of extraction at reduced costs, non-toxicity, biodegradability, anti-microbial and anti-oxidant actions, low cost, and high affinity for metallic surfaces [24,25]. Polyphenols include a wide range of natural and ubiquitous molecules in the plant world, and tannins are the most investigated polyphenols in the corrosion protection field [6,24]. Indeed, tannins' ability to scavenge oxygen radicals can be exploited to form corrosion protection films on steel surfaces by means of coordination with iron [6,26,27]. The use of

* Corresponding author. Corresponding author. auhtor.

E-mail address: marco.sangermano@polito.it (M. Sangermano).

<https://doi.org/10.1016/j.polymer.2024.127824>

Received 31 July 2024; Received in revised form 4 October 2024; Accepted 9 November 2024

Available online 12 November 2024

0032-3861/© 2024 The Author(s). Published by Elsevier Ltd. This is an open access article under the CC BY license (<http://creativecommons.org/licenses/by/4.0/>).

tannin as the main active component of anticorrosive coatings has, however, been less investigated. Moreover, due to the hydrophilic nature of tannins, their direct application as resin components for coating production can be limited. Hence, as some works already demonstrated, functionalization of phenolic moieties is necessary [28,29]. Wang et al. evaluated the corrosion protection performance of a coating modified with tannin [29]. They acrylated tannic acid (Fig. 1) with glycidyl methacrylate *via* traditional thermal procedure, which involves long reaction times. Afterwards, the acrylated tannin was extracted with an organic solvent and then introduced as an additive into a commercial petroleum-based bisphenol A epoxy acrylate resin [29]. There is a great interest to increase both the greenness of the production process and the biobased content of the coating.

In accordance with the green chemistry principles and sustainability framework, microwave irradiation is a cost-effective and eco-friendly alternative to conventional thermal and solvent-based functionalization techniques. Indeed, the modification of natural phenolic compounds *via* traditional thermal approach typically requires a solvent and catalyst, and the reaction duration can vary from 24 to 72 h to ensure effective functionalization [30–34]. Microwave-assisted processes enable more efficient energy transfer and ensure fast, volumetric, and selective heating by means of excitation of polar molecules. Furthermore, higher yields and improved purity of the products are achieved through microwave irradiation [35]. The successful microwave-assisted functionalization of phenolic moieties has been reported in the literature. Yao et al. and Truncali et al. achieved high yields of functionalized lignin with a high degree of substitution *via* microwave irradiation [36–38]. Moreover, gallic acid, a polyphenolic compound, was effectively methacrylated through a solvent-free and catalyst-free microwave-assisted technique with a yield of 90 % [39].

This research work aimed to use the microwave-assisted methacrylation reaction for the rapid production of a methacrylated tannic acid-based monomer suitable for the production of anticorrosive coatings. No previous studies report the use of tannic acid as the main active component to enable anticorrosive coating formulations with high biobased content. Moreover, the second aim was to use photopolymerization for coating low-carbon steel, because it is a sustainable and safe crosslinking method, as it ensures fast curing speed, energy saving, and no emissions of volatile organic compounds (VOCs) [23,40]. Lastly, air plasma was used as a pre-treatment on the low-carbon steel surface because it is more sustainable and safe contrary to the traditional

steel pre-treatments [19,41,42]. The corrosion protection performance of the proposed UV-cured natural polyphenol-based coating was evaluated through electrochemical tests.

2. Experimental

2.1. Materials

The extract of tara Tan'Active T80 (TA) from *Caesalpinia spinosa* was supplied by Silvateam (San Michele Mondovì, Cuneo, Italy). It consists of 100 % gallic tannins with a tannic acid content >90 %. Methacrylic anhydride (94 %, inhibited with 2.000 ppm topanol A) and phenylbis (2,4,6-trimethylbenzoyl)phosphine oxide (BAPO) were purchased from Sigma Aldrich. Chromium(III) 2,4-pentanedionate ($\text{Cr}(\text{acac})_3$, 97 %), 2-chloro-4,4,5,5-tetramethyl-1,3,2-dioxaphospholane (TMDP, 95 %), pyridine (anhydrous, 99.8 %), chloroform (≥ 99.8 %, with 0.5–1.0 % of ethanol as stabilizer), acetone (≥ 99.5 %), sodium carbonate (Na_2CO_3), Folin-Ciocalteu phenol reagent 2 M (F&C reagent), hydrochloric acid (HCl, 37 %), sodium hydroxide (NaOH, ≥ 97 %), potassium chloride (KCl, ≥ 99 %) and sodium chloride (NaCl ≥ 99 %) were also obtained from Sigma Aldrich. N-Hydroxy-5-norbornene-2,3-dicarboxylic acid imide (NHND, >99.0 %) was purchased from Tokyo Chemical Industry, and chloroform-d (99.8 %) from Cambridge Isotope Laboratories. The measuring liquid for the contact angle analysis was Water (ROMIL-SpS™ Super Purity Solvents) from ROMIL. All chemicals were used as received without further purification.

Q-PANEL® standard test substrates (ASTM A1008 [43], low-carbon steel, 0.51 mm thick, Q-Lab) were used and cut into 20 mm × 20 mm pieces. The chemical composition of these materials is (wt%): <0.15 C, <0.60 Mn, <0.03 P, <0.035 S, and bal. Fe.

2.2. Microwave-assisted methacrylation reaction of TA

Tannic acid (TA) was methacrylated in a microwave reactor, following a previous procedure [39], which was adapted from prior works [36,44]. The high-pressure Teflon vessel was filled with TA and methacrylic anhydride (MA) at a weight ratio of 1:5 TA to MA. After a thorough mixing, the vessel was subjected to microwave waves (flexiWAVE MA186-001 microwave) for isothermal heating at 130 °C for 10 min. A ramp time of 5 min and a maximum power of 1200 W were settled. Subsequently, room temperature was achieved with a cooling time of 10 min. Thereafter, to precipitate the methacrylated tannic acid (MTA), the vessel content was poured into distilled water. The resulting suspension was stirred for 24 h at room temperature followed by vacuum filtration. During the vacuum filtration, the product was washed with distilled water several times to remove the unreacted anhydride and acid by-product. Finally, after vacuum drying at room temperature for at least 48 h, the brownish and viscous liquid product of MTA was obtained.

2.3. Characterization methods

2.3.1. Nuclear magnetic resonance (NMR) spectroscopy

The quantitative analysis of tannin OH groups before and after the microwave-assisted functionalization was performed *via* Phosphorus nuclear magnetic resonance (^{31}P NMR) spectroscopy according to a previously described protocol [45]. Due to the complexity of tannins structure and their low solubility in organic solvents, ^{31}P NMR analysis is an advantageous approach to quantify and differentiate OH groups. Therefore, a phosphorylation reaction was performed on TA and MTA to evaluate the chemical shifts of the resulting phosphorylated OH groups [40,41]. About 30 mg of tannin sample was dissolved in 0.5 mL of solvent A, which was composed of chloroform-d and anhydrous pyridine with a volume ratio of 1:1.6 (vol/vol). For the internal standard solution, two solutions were prepared in solvent A and then mixed together: 5.0 mg/mL solution of the relaxing agent $\text{Cr}(\text{acac})_3$ and 18.0 mg/mL

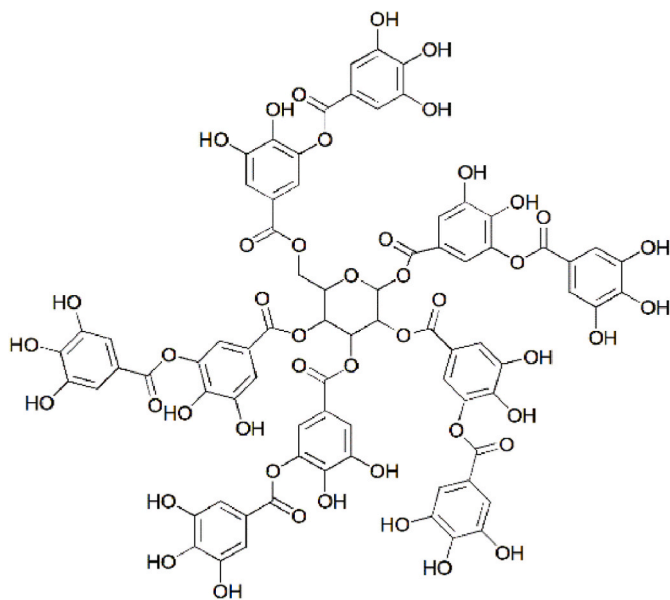


Fig. 1. Tannic acid chemical structure.

solution of the internal standard NHND. Afterwards, 0.1 mL of the internal standard solution was added to the tannin sample solution. The resulting mixture was stirred overnight. Prior to ^{31}P NMR analysis, 0.1 mL of the phosphorylating agent TMDP was added to the homogenous tannin solution and stirred for 30 s. To perform ^{31}P NMR spectroscopy, the phosphitylated tannin solution was transferred into a 5 mm NMR tube, and a Bruker Avance III HD 400 MHz spectrometer was used. A relaxation delay of 2 s and 1024 scans were included in the acquisition parameters. The resulting data were processed by means of MestReNova software (Mastrelab Research SL), and phase corrections and automatic baseline were applied. The chemical shift was calibrated to the reference signal of the product of TMDP and water at 132.2 ppm. The determination of hydroxy group content on TA and MTA was achieved by integration of peak regions attributed to OH groups. In detail, the used integration regions were: aliphatic OH (149.0–147.0 ppm), phenolic OH (144.0–138.8 ppm) and carboxylic acid OH (133.6–136.0 ppm) [45,46]. Derived integral values were converted to mmol OH/g tannin in accordance with Equation (1):

$$\text{mmol OH} / \text{g tannin} = \frac{R \times \text{NHND in NMR sample [mmol]}}{\text{Dry weight of tannin [g]}} \quad (1)$$

Where R is the integral ratio of the ^{31}P NMR region of interest over the region of the internal standard.

The degree of substitution (DS) was estimated following Equation (2):

$$\text{DS} = \frac{C(\text{OH})_i [\text{mmol/g}] - C(\text{OH})_f [\text{mmol/g}]}{C(\text{OH})_i [\text{mmol/g}] + C(\text{OH})_f [\text{mmol/g}] \times \Delta m_{\text{max}}} \quad (2)$$

In which $C(\text{OH})_i$ and $C(\text{OH})_f$ are the initial and final concentrations of OH units in tannin, respectively, and Δm_{max} is the weight increased per g of tannin at 100 % conversion.

2.3.2. Folin-Ciocalteu (F&C) assay

The total phenolic concentration of MTA was assessed by the Folin–Ciocalteu (F&C) assay [47]. The test is based on the reduction of the F&C reagent caused by the oxidation of the phenolic compounds [48]. After the dipping in 8 mL of double-distilled water, 0.5 mL of F&C reagent and 1.5 mL of 20 w/v% Na_2CO_3 solution were added. Thus, the reaction between the phenols in MTA and phosphor-tungstic/phosphomolybdic acid contained in the F&C reagent was carried out for 2 h in the dark. The photometric tests were performed by measuring the solution's absorbance at 760 nm with a UV–Vis spectrophotometer (UV-2600, Shimadzu, Japan). The content of total phenols was quantified according to a standard calibration curve of gallic acid, obtained by seven solutions with established concentrations (0.001, 0.003, 0.005, 0.010, 0.020, 0.030, and 0.040 mg/mL). The phenol content of MTA was quantified by using gallic equivalent units (GAE) as a measuring unit.

2.3.3. Fourier transform infrared (FTIR) spectroscopy

The structural changes before and after methacrylation reaction were assessed by using a PerkinElmer Spectrum 100 instrument (PerkinElmer Waltham, Massachusetts, US), in an attenuated total reflection (ATR) mode, equipped with a diamond crystal. The ATR-FTIR spectra were acquired with a resolution of 4 cm^{-1} and obtained as the average of 16 scans.

In order to investigate the effect of the concentration of BAPO photoinitiator on UV-curing process of the synthesized MTA, a Thermo Scientific Nicolet iS50 FTIR spectrometer (Thermo Fisher Scientific, Milano, Italy) was used. The BAPO content was varied from 1 to 3 phr (per hundred resin). The liquid formulation was spread on a silicon wafer by a film bar to obtain a thickness of 12 μm . The sample was irradiated by UV light under N_2 flow, exploiting a Hamamatsu LC8 lamp with an 8 mm light guide and spectral distribution range of 240–400 nm. The real-time FTIR spectra were collected in the range of 4000–600

cm^{-1} with a spectral resolution of 4.0 cm^{-1} and resulted in 32 scans. The conversion degree was estimated by the disappearance of the $\text{C}=\text{C}$ peak at 1634 cm^{-1} [49,50], while the $\text{C}=\text{O}$ signal at 1740 cm^{-1} was assumed to be unaffected by UV-light irradiation [19,51]. All measurements were carried out in triplicate. The conversion degree was calculated according to Equation (3).

$$\text{Conversion degree [\%]} = \frac{\left(\frac{A_{\text{C}=\text{C}}}{A_{\text{C}=\text{O}}}\right)_{t=0} - \left(\frac{A_{\text{C}=\text{C}}}{A_{\text{C}=\text{O}}}\right)_t}{\left(\frac{A_{\text{C}=\text{C}}}{A_{\text{C}=\text{O}}}\right)_{t=0}} \times 100 \quad (3)$$

where $A_{\text{C}=\text{C}}$ and $A_{\text{C}=\text{O}}$ are the areas of the peak assigned to the stretching vibrations of the methacrylic double bonds and the reference peak, respectively, measured at different times.

2.3.4. Differential scanning photo calorimetry (photo-DSC) and differential scanning calorimetry (DSC)

To investigate the photocrosslinking process, the differential scanning photo calorimetry (photo-DSC) was performed by using a Mettler Toledo DSC-1 instrument equipped with Gas Controller GC100 (Mettler Toledo Columbus, Ohio, US). A mercury lamp (Hamamatsu Lightning-cure™ LC8, Hamamatsu Photonics) with an optical fiber to directly irradiate the sample with a UV light emission centered at 365 nm and intensity at 100 % was used. About 5–10 mg of the UV-curable liquid formulation with different amount of BAPO photoinitiator (1, 2 and 3 phr) was poured into an open 40 μL aluminum pan. The reference was an empty pan. The experiments were carried out at room temperature ($25 \text{ }^\circ\text{C}$) under N_2 atmosphere with a flow rate of 40 mLmin^{-1} . The samples were subjected to UV irradiation two times for 5 min. The second UV light exposure step was required to confirm the complete UV-curing and establish the baseline. The curing curve resulted from the subtraction of the second curve from the first one.

The differential scanning calorimetric (DSC) analysis was carried out on 5–10 mg of UV-cured MTA in 40 μL aluminum pan and covered with a pierced lid. The heating/cooling method was performed with a heating/cooling rate of 10 Kmin^{-1} and under N_2 flow (40 mL min^{-1}) and composed of five steps. The sample was firstly heated from $-20 \text{ }^\circ\text{C}$ to $200 \text{ }^\circ\text{C}$; after the cooling to $-20 \text{ }^\circ\text{C}$, the chamber was heated to $250 \text{ }^\circ\text{C}$ and subsequently again cooled to $-20 \text{ }^\circ\text{C}$; finally, the sample was heated until $300 \text{ }^\circ\text{C}$. The glass transition temperature (T_g) was estimated from the third heating.

All tests were carried out in triplicate and the data were elaborated by Mettler STARE software V9.2.

2.3.5. Photo-rheological measurement

An Anton Paar Modular Compact rheometer (Physica MCR 302, Graz, Austria) was used to investigate the photo-rheological behaviours of the MTA formulation with 3 phr of photoinitiator. A plate-plate geometry with plates measuring 25 mm in diameter was set. The distance between the two plates was 0.3 mm and an oscillatory condition at frequency of 1 Hz was used. A Hamamatsu Lightningcure™ LC8 lamp (Hamamatsu Photonics, Shizuoka, Japan) with a broad UV spectrum centered at 365 nm was employed as a light source. The lamp was positioned beneath the bottom plate and it was turned on after 60 s with a light intensity of 100 mW/cm^2 . The photo-rheology was assessed as a function of the changes in the storage modulus (G') and in the loss modulus (G'') of the sample versus the exposure time. The onset of the gel formation was evaluated as gelation time (t_{gel}), which is considered as the time where $G' = G''$ or the loss factor $\tan \delta$ (G''/G') [52]. The crosslinking density was estimated using Equation (4) [53]:

$$\nu_e = \frac{G' [\text{Pa}] N_A [\text{mol}^{-1}]}{R [\text{m}^3 \text{PaK}^{-1} \text{mol}^{-1}] T [\text{K}]} \quad (4)$$

where G' is the storage modulus in the plateau region of the photo-

rheological curve, N_a is the Avogadro number, R is the gas constant and T is the working temperature (25 °C). All the measurements were carried out in triplicate at room temperature.

2.3.6. Gel content

The gel content percentage (%gel) was estimated on UV-cured MTA with 3 phr of photoinitiator. Around 100 mg of sample was immersed in chloroform for 24 h and, after drying in air for further 24 h, the weight loss was measured to determine the gel according to Equation (5).

$$\%gel = \frac{W_f [g]}{W_i [g]} \times 100 \quad (5)$$

where W_i and W_f are the weights of the dry sample before and after the extraction, respectively.

2.3.7. Thermogravimetric analysis (TGA)

The thermal stability of UV-cured MTA was assessed by thermogravimetric analysis (TGA). A Mettler-Toledo TGA 851e instrument (Mettler Toledo, Columbus, Ohio, US) was exploited. The sample was heated from 25 °C to 800 °C with a heating rate of 10 °C min⁻¹ under Ar atmosphere with a flow of 50 mL min⁻¹. All curves were normalized to the unit weight of the samples.

2.3.8. Zeta potential

The zeta (ζ) potential was assessed on the surface of UV-cured MTA as a function of pH in an electrolyte solution of 0.001 M KCl by using an electrokinetic analyzer (SurPASS, Anton Paar, Graz, Austria) equipped with an automatic titration unit and an adjustable gap cell. The pH was changed by the addition of 0.05 M HCl and 0.05 M NaOH solutions for titration in the acid and alkaline range, respectively. Fifteen points were acquired for each range, and four ramps were conducted for each point. Between the two measurements, the sample was thoroughly rinsed with ultrapure water to use the same sample for basic and acid titrations.

2.4. Preparation and characterization of MTA coating

Before the application of MTA coating, the surface of low-carbon steel substrates (Q-PANEL®) was pre-treated to remove any impurities, such as carbon contaminants or rust formed during the steel's storage. Firstly, steel samples were degreased by sonification in acetone for 5 min at room temperature. The steel surface was treated with an air plasma (Tucano, Gambetti Kenologia, Binasco, MI, Italy) at 100 W for 10 min. Afterwards, the steel substrates were immediately coated by the MTA coating formulation.

The coating formulation was composed of MTA and 3 phr of BAPO as radical photoinitiator. The plasma pre-treated steel substrates were coated by MTA coating with 100 μ m in thickness by using a film bar. The coated steel samples were irradiated by UV light at room temperature for 5 min. Inert atmosphere was used to avoid the quenching by oxygen. A Dymax ECE 5000 with a light intensity of 130 mW/cm² with an emission ranged from 275 to 500 nm with a maximum intensity at 365 nm was employed.

2.4.1. Contact angle analysis

The wettability of the MTA coating was assessed by means of a drop shape analyzer (DSA100, Krüss, Hamburg, Germany) equipped with a video camera. The contact angle analysis was conducted at room temperature through the sessile drop technique placing the 5 μ L water droplet on a free surface of the coating. The measurements were repeated three to six times.

2.4.2. Hardness tests

The hardness of the MTA coating was evaluated through two different tests. Firstly, the Sauter HMO mobile Leeb Hardness Tester was used by following the ASTM A956/A956 M standard [54]. The second

test was performed by using a Shore D indentation instrument according to the ASTM2240 [55]. Three measurements were performed to have an average value.

2.4.3. Electrochemical impedance spectroscopy (EIS)

Finally, the protective properties of the MTA coating were evaluated using Electrochemical Impedance Spectroscopy (EIS). The measurements were performed with a Parstat 2273 potentiostat (Princeton Applied Research by AMETEK, Oak Ridge, TN, USA) using PowerSuit ZSimpWin software (version 2.40). An input signal with an amplitude of approximately 15 mV (peak-to-peak) was applied over a frequency range of 10⁵ to 10⁻² Hz. The experimental setup included an Ag/AgCl reference electrode (+207 mV SHE) and a platinum counter electrode, both immersed in a 3.5 wt% sodium chloride solution. The samples remained immersed in the solution for a maximum of 168 h, with a testing area of 1.0 cm². The measurements were conducted on four samples.

3. Results and discussion

3.1. Synthesis of methacrylated tannic acid

The methacrylation functionalization of tannic acid (TA, Fig. 1) was achieved by exploiting a microwave-assisted reaction (Fig. 2). The method was based on prior works about the acetylation and methacrylation of lignin, which assessed the optimal experimental conditions to maximized the degree of substitution (DS) and the reaction product yield [36,37]. Yao et al. assessed the yield and the DS of the modified lignin as a function of different reaction parameters, and the highest values were achieved after heating of 130 °C in 10 min via microwave irradiation [36]. Moreover, the microwave-assisted methacrylation reaction at 130 °C for 10 min was previously successfully investigated for functionalization of gallic acid [39], which is a structural constituent of TA [56]. [36,37] Hence, according to the above-mentioned investigations, the functionalization of TA was carried out at 130 °C for 10 min under microwave irradiation, achieving a yield of methacrylated tannic acid (MTA) of about 88 %. By means of conventional thermal process, similar yield values of methacrylated TA were achieved after 24 or 48 h, as demonstrated by the works about methacrylation reaction in organic solvent with glycidyl methacrylate as acrylating agent in the presence of a catalyst [32,33]. Instead, the microwave-assisted methacrylation reaction of TA was demonstrated solvent-free and catalyst-free in the present study. Therefore, the functionalization via microwave irradiation technique was successfully performed in remarkably short reaction time and at a moderate temperature.

The conversion of OH groups into methacrylate moieties was quantified by ³¹P NMR spectroscopy (Fig. 3a).

What emerges from the ³¹P NMR spectra is a significant decrease of the area of the phenolic alcohol region (144.0–138.8 ppm). Indeed, the TA's phenolic moieties were almost fully methacrylated, reaching a DS of 91 %. In addition, the presence of aliphatic (149.0–147.0 ppm) and carboxylic OH (133.6–136.0 ppm) groups in the ³¹P NMR spectrum of TA can be attributed to impurities resulting from the extracting process of TA from *Caesalpinia spinosa*. The peaks of carboxylic OH groups were detectable also in the ³¹P NMR spectrum of MTA due to the acid by-product (methacrylic acid). Table 1 reports the content of OH groups before and after the microwave-assisted functionalization. The incomplete methacrylation of TA can have several effects. Free polyphenolic groups on the side of the coating toward the substrate are available for coordinating iron ions of steel, as the F&C test also demonstrated, and can increase the adhesion to the substrate. Moreover, the unmodified OH groups inside the coating could be involved in hydrogen bonds during the polymerization, enhancing the crosslinking density, and thus mechanically reinforcing the MTA coating. Lastly, the OH groups exposed outwards can increase the corrosion protection (see 3.5). Indeed, a concentration of total phenols in MTA sample of 0.082 mg/mL

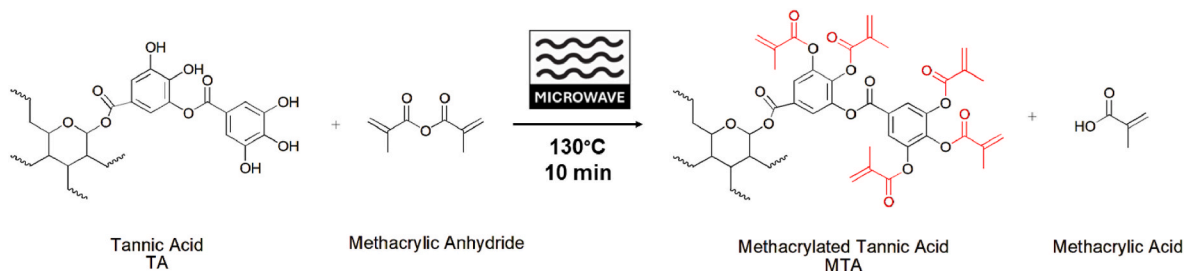


Fig. 2. Simplified schematization of the microwave-assisted methacrylation of tannic acid by methacrylic anhydride, which implies the production of methacrylic acid as a by-product.

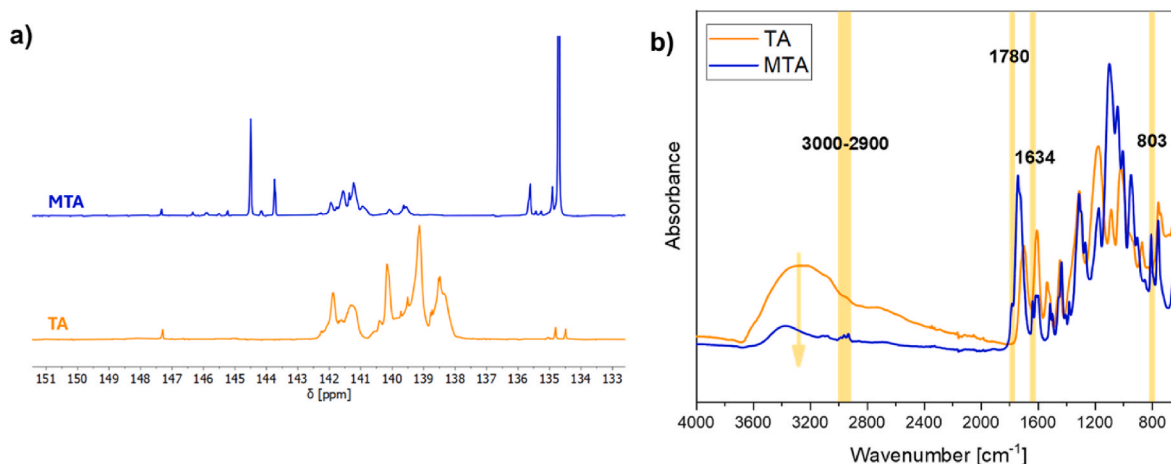


Fig. 3. a) ^{31}P NMR spectra of tannic sample before (TA) and after methacrylation reaction (MTA); b) ATR-FTIR spectra of TA and MTA.

Table 1

Quantification of hydroxy groups content on TA and MTA according to Equation (1).

Sample	Phenolic OH [mmol/g]	Carboxylic OH [mmol/g]	Aliphatic OH [mmol/g]	Total OH [mmol/g]
TA	101.2	1.414	1.357	103.6
MTA	8.991	12.50	2.466	23.95

± 0.006 was measured by F&C assay.

The methacrylation of TA *via* microwave-assisted process was further monitored by ATR-FTIR analysis (Fig. 3b). Firstly, the evident and significant decrease in intensity of the band assigned to OH groups' stretches suggested the consumption of TA's phenolic alcohol groups due to the functionalization. The appearance of the new peaks at 1634 and 803 cm^{-1} , corresponding to C=C stretches and in-plane C=CH₂ bend, respectively, assured the effective methacrylation reaction. Furthermore, a slight shoulder at 1780 cm^{-1} is noticeable in FTIR spectrum of MTA and was related to the stretching vibrations of the methacrylic C=O groups. Lastly, the signals in the wavenumber region of 3000–2900 cm^{-1} due to the stretches of the methacrylic methyl groups were observed in the spectrum of MTA.

Therefore, the structural characterization of MTA by both ^{31}P NMR and ATR-FTIR spectroscopies fully supported the successful microwave-assisted methacrylation.

3.2. Photopolymerization kinetics

The photopolymerization process of MTA was monitored through real-time FTIR, photo-DSC analyses, and photo-rheological measurement.

The conversion of photocurable methacrylate moieties in MTA was investigated as a function of UV light irradiation by means of real-time FTIR spectroscopy. The FTIR spectra of MTA before and after UV-curing are collected in Fig. 4. It is evident that, after 180 s of irradiation, the intensity of the signal at 1634 cm^{-1} attributed to the double bonds C=C of methacrylate moieties, was significantly decreased because of the radical photocrosslinking process.

Moreover, the influence of the radical photoinitiator content in the UV-curable MTA formulation on the final MTA conversion degree and photocrosslinking rate was assessed. Conversion curves as a function of UV light irradiation time for MTA formulations with different BAPO content were determined by following the decrease of the area of the signal at 1634 cm^{-1} (Fig. 5).

The final conversion moderately increased as the concentration of the radical photoinitiator increased, as Table 2 reports. The observed increment in the conversion degree can be explained by the higher amounts of photogenerated radicals from the photoinitiator during the irradiation. Indeed, more radicals are available to initiate the photopolymerization, enhancing also the UV-curing kinetics (Table 2) [21]. All three MTA formulations reached conversions from 74 to 80 % after 180 s of irradiation.

Photo-DSC analysis on the same MTA formulations with different BAPO contents and under the same temperature curing conditions, i.e. 25 °C, corroborated the real-time FTIR results. The photo-DSC curves are shown in Fig. 6. Table 3 collects the significant parameters extrapolated from photo-DSC experiments: the time at maximum rate of crosslinking (t_{peak}), the peak height at maximum of the DSC curve (h_{peak}), and the heat release (ΔH), estimated as the total enthalpy from the curing peak integration. What stands out from photo-DSC analysis is that the t_{peak} decreased as the BAPO concentration increased, confirming a faster photocrosslinking process with higher amount of photoinitiator. In detail, taking into consideration the standard deviations, the values of

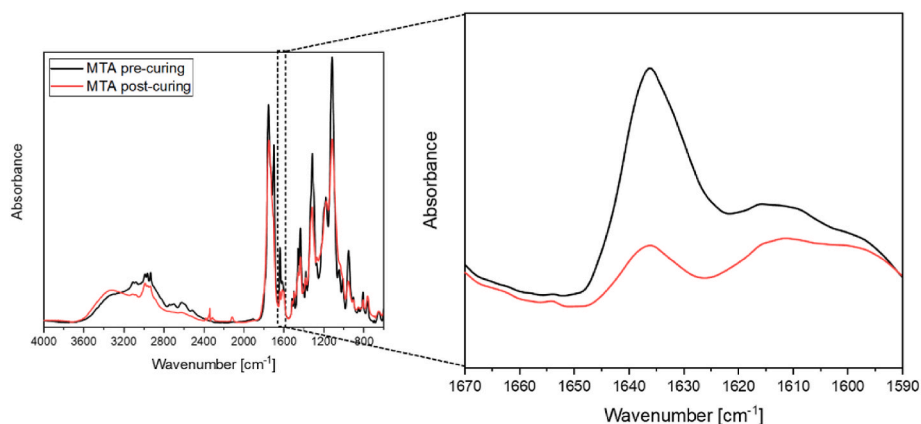


Fig. 4. Real-time FTIR spectra of MTA formulation with 3 phr of BAPO photoinitiator before (pre-curing) and after (post-curing) UV light irradiation for 180 s.

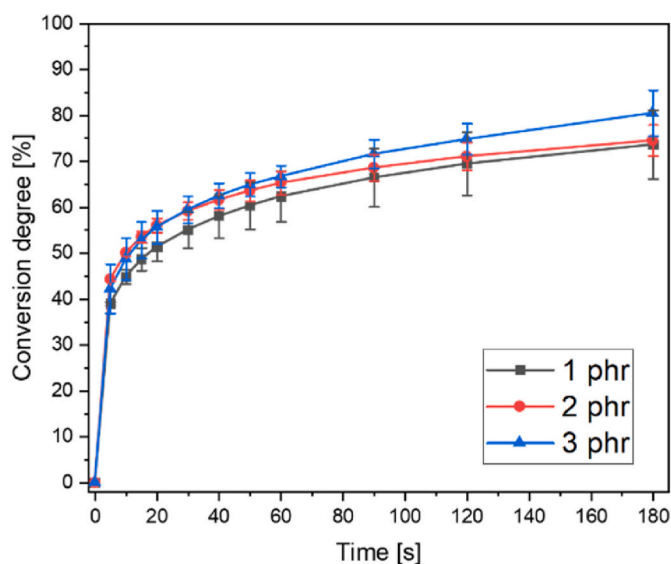


Fig. 5. Conversion curves for MTA formulations with 1, 2, and 3 phr of the radical photoinitiator.

Table 2

Conversion degrees, estimated by Equation (3), of MTA formulations with different BAPO concentrations after specified time of UV light irradiation.

BAPO concentration	Conversion degree [%] after 5 s	Conversion degree [%] after 30 s	Conversion degree [%] after 60 s	Conversion degree [%] after 180 s
1 phr	39 ± 0.3	55 ± 4	62 ± 6	74 ± 7
2 phr	44 ± 0.3	59 ± 2	65 ± 2	74 ± 3
3 phr	42 ± 5	59 ± 3	67 ± 2	80 ± 5

h_{peak} and ΔH of the MTA formulations with 2 phr and 3 phr of BAPO were comparable, proving the high photo-reactivity of the systems. Therefore, from the results of the real-time FTIR and photo-DSC analyses, the addition of 3 phr of the radical photoinitiator was chosen for the subsequent investigations and for the coating preparation.

In addition to real-time FTIR and photo-DSC analyses, a further investigation of the UV-curing process of MTA was conducted by means of real-time photo-rheology. The increase of the storage modulus results from the crosslinking reaction. As can be seen in Fig. 7, the UV lamp was turned on after 60 s of darkness and the UV light irradiation almost immediately increased the storage modulus in only 20 s. The gelation time (t_{gel}) at 2.5 s confirmed the high photo-reactivity of MTA. After 80 s

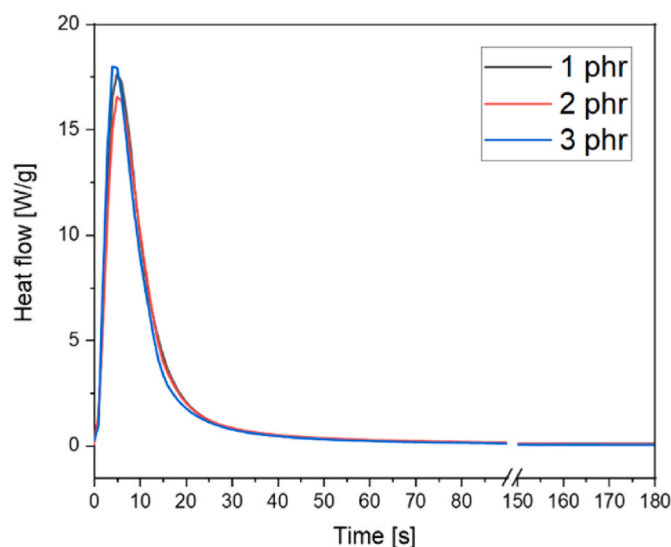


Fig. 6. Photo-DSC curves for MTA formulations with 1, 2, and 3 phr of BAPO.

Table 3

Photo-DSC results of MTA formulations with different radical photoinitiator's content.

BAPO concentration	t_{peak} [s]	h_{peak} [W/g]	ΔH [J/g]
1 phr	5.3 ± 0.6	13.9 ± 7.6	138.9 ± 72.9
2 phr	5.0 ± 1.0	17.87 ± 3.9	177.5 ± 7.5
3 phr	5.0 ± 1.0	16.6 ± 1.8	176.5 ± 12.1

the photo-rheological curve reached the plateau once the photopolymerization reaction was terminated reaching crosslinking density (ν_e) of $1.19 \times 10^{27} \text{ m}^{-3}$.

Lastly, the gel fraction of MTA after the UV-curing process was assessed by 24 h extraction in chloroform. A gel content (%gel) of 99 ± 0.2 was measured. This outstanding %gel value was in accordance with the high conversion degree and revealed the efficient formation of insoluble fraction due to the crosslinks formed between MTA monomers.

3.3. Thermal analysis of UV-cured MTA

The glass transition temperature (T_g) of the UV-cured MTA was estimated by DSC analysis. As shown in Fig. 8a, the UV-cured methacrylated tannin exhibited a very high T_g value of about 133 °C. Therefore, a significant crosslinking of the photo-crosslinked MTA was

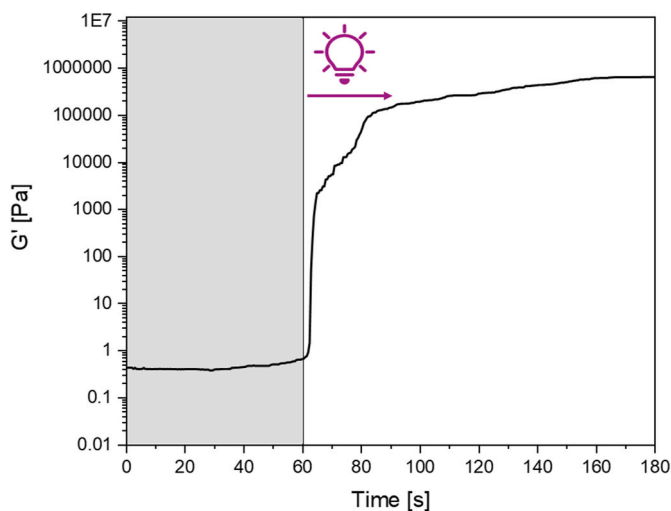


Fig. 7. Photo-rheology with 3 phr of radical photoinitiator.

implied. This outstanding result correlates with the T_g of methacrylated gallic acid [39], and its thermoset [57,58]. Finally, a high T_g implies a decrease in oxygen and water permeability, and thus an enhancement in the protective barrier properties of the coating [59,60].

In addition, TGA experiments in inert atmosphere were carried out to investigate the thermal stability of UV-cured MTA. The TGA thermogram is reported in Fig. 8b and showed a two-step degradation profile. The first stage was between 165 °C and 328 °C and could be related to the decomposition of not completely cured MTA, like dangling chain ends. The second step (328–500 °C) occurred at remarkably high temperature probably due to the degradation of the phenolic moieties and the random scission of crosslinked chains [37,61,62]. The thermal degradation temperature of 20 % mass loss ($T_{deg20\%}$) was approximately 282 °C, and the char yield (w_{char}) was around 14 %. Hence, the assessed high thermal stability of MTA-based cured polymer can be explained by the high crosslinking density and aromatic content.

3.4. Surface properties of UV-cured MTA

The correlation between the corrosion resistance of a coating and its surface wettability is noteworthy [6,17,63–69]. Thus, the water contact angle on UV-cured MTA coating was assessed and a value of $75^\circ \pm 2$ was measured. The hydrophobicity of the coating is explained by the introduction of the methacrylate moieties, which consumed most of the hydrophilic phenolic alcohol-groups of TA.

Moreover, hardness plays a crucial role in the durability of the material [70,71]. The hardness of MTA coating was assessed by Leeb rebound hardness and the Shore D hardness tests. Both of the hardness measurements estimated good hardness values for UV-cured MTA: 525

± 41 of Leeb hardness and 70 ± 5 of Shore D hardness. The rigidity of the polymeric network can explain these results, implying high cross-linking density and aromatic content for the tannin-based coating, as suggested by the high T_g values. Commercially available acrylic resins generally show a Leeb hardness in the range of 750–811 [71]. Therefore, the proposed UV-cured bio-based coating exhibited a value of Leeb hardness not remarkably different and lower from commercial acrylic resins. Furthermore, the evaluated Shore D hardness proved to be higher than the values reported for UV-cured castor oil-based hyperbranched acrylate coatings (25–50 Shore D hardness) [72], and the value was also higher or comparable with hardnesses of other reported bio-based coatings [73–75].

Finally, since during the corrosion process ions in the electrolyte have a significant impact on the corrosive deterioration of metals, the surface charge density of MTA coating was investigated by means of zeta (ζ) potential measurement. As Fig. 9 displays, the UV-cured MTA showed a predominantly negative surface charge at the pH range studied due to the acidic polyphenolic OH and ester groups. The isoelectric point (IEP) was measured at an extreme acidic pH of 2.7. Overall, as can be seen from the standard deviation values for each point in Fig. 9, the system was chemically stable to pH changes. The correlation between the ζ potential and the corrosion process has been previously investigated. Indeed, the literature reports that the negative ζ potential proved to discourage chloride adsorption under the effect of electrostatic force, and thus the anodic film was less susceptible to chloride attack [76–78].

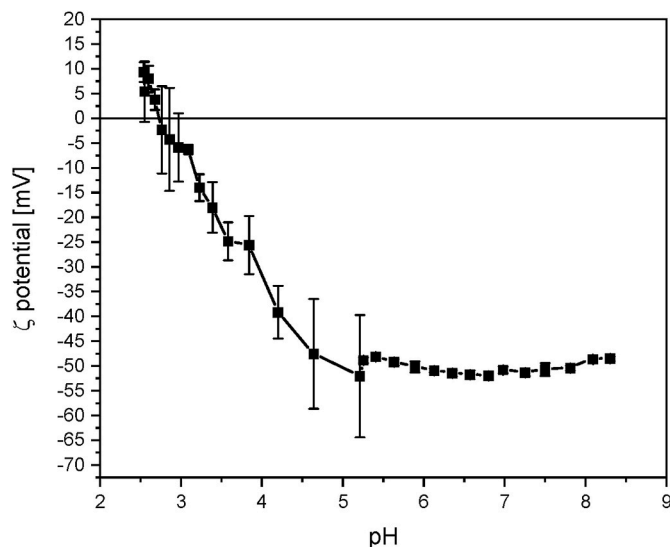


Fig. 9. ζ potential curve of UV-cured MTA.

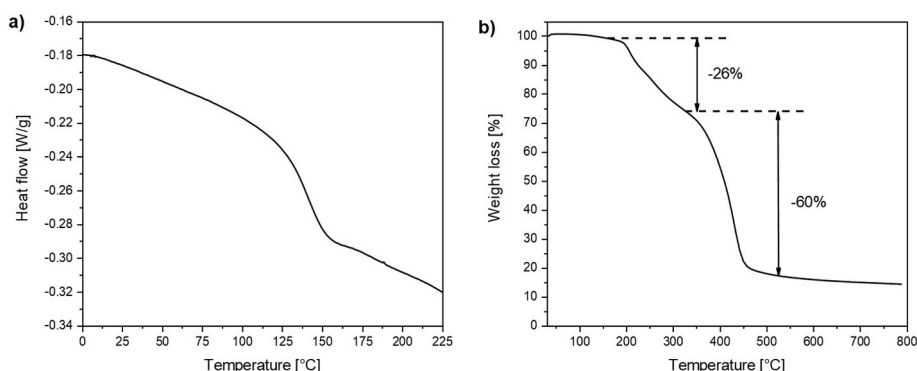


Fig. 8. a) DSC and b) TGA thermogram of UV-cured MTA with 3 phr of BAPO photoinitiator.

3.5. Anticorrosion performance of the UV-cured MTA coating

In order to assess the corrosion protection performance of the UV-cured MTA coating, possible contaminants and scale on the surface of low-carbon steel were removed by means of air-plasma process. Plasma pre-treatment is an eco-friendly and highly efficient technique to enhance the metallic surface reactivity towards coatings [41,79,80]. Thus, plasma irradiation can be a more sustainable and alternative process to conventional ones, like pickling methods, which require extensive use of strong inorganic acids [19,81].

Accordingly, the protective capabilities of the MTA coatings were assessed through electrochemical impedance spectroscopy (EIS) measurements. EIS is a commonly employed method for evaluating the protective characteristics of organic coatings [82], including their defectiveness or degree of adhesion [83]. The Bode impedance modulus at low frequencies (10^{-2} Hz), denoted as $|Z|_{(0,01)}$, provides a rough quantitative estimate of the protective effectiveness of the coating. Several studies in the literature establish that a $|Z|_{(0,01)}$ value of $10^6 \Omega \text{ cm}^2$ is the minimum threshold for a coating to be considered as “protective” [84–86].

Fig. 10a illustrates the trend of $|Z|_{(0,01)}$ over time for four replicates of MTA coating on low-carbon steel. The graph reveals variations among the samples, although all exhibited the same decreasing trend typical of EIS measurements, which indicates the development of degradation of the coating and the starting of corrosive phenomena [87]. Generally, at the first time of immersion, the four samples demonstrated good protective performance, with $|Z|_{(0,01)}$ values remaining relatively high. The main difference was in the initial values; for instance, the $|Z|_{(0,01)}$ value of MTA1 sample started at nearly $10^9 \Omega \text{ cm}^2$, while the MTA2 sample began almost two orders of magnitude lower. This variation was likely due to the differences in the integrity of the coatings, with MTA1 appearing compact and defect-free to the ‘system’, while MTA2 likely showed noticeable defects from the outset. The MTA3 and MTA4 samples displayed intermediate behaviour between these two extremes. When free of significant defects, as in the case of the MTA1 sample, the coating exhibited excellent protective properties. This is attributed to the strong adhesion between the coating layer and the metal substrate, facilitated by the incomplete methacrylation of TA shown by ^{31}P NMR measurements. The residual free polyphenolic groups in TA are expected to coordinate with the surface iron ions of the steel.

The reduction trend of $|Z|_{(0,01)}$ over time was likely due to the penetration of the solution into the coating. To further investigate this phenomenon, Fig. 10b displays the evolution of the Nyquist diagrams for the MTA1 sample. At $t = 0$ h, the curve tends to close on itself, indicating a continuously evolving “system”. This suggests that the coating was slowly absorbing the test solution due to intrinsic porosity. After 24 h, two ‘time constants’ become evident, represented by two semicircles in the Nyquist curve. The first semicircle at high frequencies indicates dissipation phenomena caused by the protective layer, while the second semicircle at low frequencies indicates dissipation processes occurring at the interface with the metal substrate [88]. This was a result

of the solution percolating through the coating, leading to initial corrosion phenomena on the steel surface.

In fact, the most significant drop in $|Z|_{(0,01)}$ shown in Fig. 10a occurred within the first 24 h of the measurements. After this initial period, despite the dissipation processes at the interface, the strong adhesion of the MTA layer prevents significant delamination. Consequently, the reduction in $|Z|_{(0,01)}$ and thus the decline in protective properties happened very gradually.

Ultimately, it can be concluded that UV-cured MTA layer provided an effective solution for protecting metal substrates. However, the decreasing trend of $|Z|_{(0,01)}$ values over time for all samples, particularly for samples MTA2 and MTA4, which show values below the threshold of $10^6 \Omega \text{ cm}^2$ that allows an organic coating to be considered protective [85,86], highlights a certain criticality in the studied samples. It is therefore necessary to optimize the production process to reduce the porosity and defects in the layers.

The performance of the coating can be further enhanced by reducing porosity and minimizing defects during the deposition process. The analyses have demonstrated that the incomplete methacrylation of TA could be important for good adhesion to the metal substrate, offering promising results for the development of sustainable organic coatings. Moreover, the remaining free OH groups in MTA can contribute to the corrosion protection on steel thanks to their ability to scavenge oxygen radicals [6,26,89,90].

4. Conclusions

Microwave-assisted functionalization of natural extract of tannic acid (TA) was successfully demonstrated. The reaction led to a high-yield and high degree of substitution in significantly reduced reaction time without additional solvents and catalysts.

The methacrylated tannic acid (MTA) was successfully radically photopolymerized achieving a conversion degree of 80 % with 3 phr of photoinitiator after 180 s of UV light irradiation. The high photo-reactivity of MTA was further confirmed by the short gelation time and produced a notably high insoluble fraction. Furthermore, the UV-cured MTA showed elevated T_g and good thermal stability.

Finally, the photopolymerized MTA was demonstrated as a potentially eco-friendly coating for low-carbon steel with very low wettability and good hardness. Moreover, a sustainable plasma pre-treatment of steel surface before applying the MTA coating proved to be efficient. Preliminary EIS measurements indicated promising potential in terms of protective performance, with $|Z|_{(0,01)}$ values consistently exceeding the critical threshold of $10^6 \Omega \text{ cm}^2$ even after one week of exposure to an aggressive solution. From EIS results, a further degradation of the metal substrate might be mitigated by the good adhesion of the MTA coating. However, the results also denoted challenges related to the percolation of the solution into the surface layer.

In conclusion, a more sustainable anticorrosive coating based on natural tannins *via* greener functionalization, surface treatment, and photopolymerization methods was demonstrated.

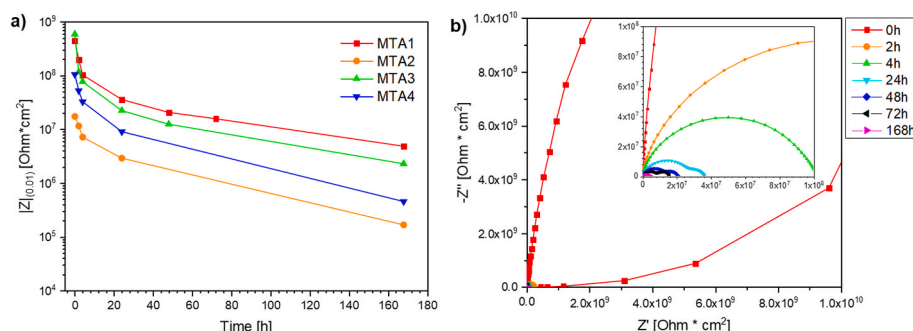


Fig. 10. a) Evolution of Bode impedance modulus $|Z|_{(0,01)}$ over time and b) relative Nyquist diagram of sample MTA1.

CRedit authorship contribution statement

Rossella Sesia: Methodology, Investigation. **Paula Pou I Rodríguez:** Investigation. **Massimo Calovi:** Investigation. **Minna Hakkarainen:** Data curation, Conceptualization. **Stefano Rossi:** Formal analysis. **Sara Ferraris:** Funding acquisition, Data curation. **Silvia Spriano:** Funding acquisition, Conceptualization. **Marco Sangermano:** Funding acquisition, Data curation.

Declaration of competing interest

The authors declare that they have no known competing financial interests or personal relationships that could have appeared to influence the work reported in this paper.

Acknowledgements

MUR is acknowledged for funding R. Sesia's Ph.D. fellowship (MUR – D.M.1061/2021 – Dottorati di ricerca su tematiche green e dell'innovazione: nuove risorse dal PON Ricerca e Innovazione). Silvateam is acknowledged for the collaboration. This research was partially founded with European Union's Horizon2020 research and innovation program under the Marie Skłodowska-Curie grant agreement, No101085759 (SURE-Poly). The Authors gratefully thank Giovanna Colucci and Matilde Porcarello for TGA and photo-rheological measurements, respectively.

Data availability

Data will be made available on request.

References

- D. Dwivedi, K. Lepková, T. Becker, Carbon steel corrosion: a review of key surface properties and characterization methods, *RSC Adv.* 7 (2017) 4580–4610, <https://doi.org/10.1039/C6RA25094G>.
- H. Gerengi, N. Sen, I. Uygur, M.M. Solomon, Corrosion response of ultra-high strength steels used for automotive applications, *Mater. Res. Express* 6 (2019) 0865a6, <https://doi.org/10.1088/2053-1591/ab2178>.
- G. Koch, Cost of corrosion, in: *Trends in Oil and Gas Corrosion Research and Technologies*, Elsevier, 2017, pp. 3–30, <https://doi.org/10.1016/B978-0-08-101105-8.00001-2>.
- J.Y. Hu, S.S. Zhang, E. Chen, W.G. Li, A review on corrosion detection and protection of existing reinforced concrete (RC) structures, *Construct. Build. Mater.* 325 (2022) 126718, <https://doi.org/10.1016/j.conbuildmat.2022.126718>.
- M. Iannuzzi, G.S. Frankel, The carbon footprint of steel corrosion, *npj Mater. Degrad.* 6 (2022) 101, <https://doi.org/10.1038/s41529-022-00318-1>.
- R. Sesia, S. Spriano, M. Sangermano, S. Ferraris, Natural polyphenols and the corrosion protection of steel: recent advances and future perspectives for green and promising strategies, *Metals* 13 (2023) 1070, <https://doi.org/10.3390/met13061070>.
- B. Liu, J. Li, W. Guo, P. Xu, S. Zhang, Y. Zhang, Progress in corrosion-resistant coatings on surface of low alloy steel, *J. Iron Steel Res. Int.* (2022), <https://doi.org/10.1007/s42243-022-00872-7>.
- M.F. Montemor, Functional and smart coatings for corrosion protection: a review of recent advances, *Surf. Coat. Technol.* 258 (2014) 17–37, <https://doi.org/10.1016/j.surfcoat.2014.06.031>.
- K. Pulidindi, M.S. Pulidindi, Global market insights. <https://www.gminsights.com/industry-analysis/anti-corrosion-coatings-market>, 2021.
- S.B. Lyon, R. Bingham, D.J. Mills, Advances in corrosion protection by organic coatings: what we know and what we would like to know, *Prog. Org. Coating* 102 (2017) 2–7, <https://doi.org/10.1016/j.porgcoat.2016.04.030>.
- J. Mu, F. Gao, G. Cui, S. Wang, S. Tang, Z. Li, A comprehensive review of anticorrosive graphene-composite coatings, *Prog. Org. Coating* 157 (2021) 106321, <https://doi.org/10.1016/j.porgcoat.2021.106321>.
- N. Attarzadeh, M. Molaei, K. Babaei, A. Fattah-alhosseini, New promising ceramic coatings for corrosion and wear protection of steels: a review, *Surface. Interfac.* 23 (2021) 100997, <https://doi.org/10.1016/j.surfin.2021.100997>.
- C. Verma, L.O. Olasunkanmi, E.D. Akpan, M.A. Quraishi, O. Dagdag, M. El Gouri, E.-S.M. Sherif, E.E. Ebenso, Epoxy resins as anticorrosive polymeric materials: a review, *React. Funct. Polym.* 156 (2020) 104741, <https://doi.org/10.1016/j.reactfunctpolym.2020.104741>.
- G. Cui, Z. Bi, S. Wang, J. Liu, X. Xing, Z. Li, B. Wang, A comprehensive review on smart anti-corrosive coatings, *Prog. Org. Coating* 148 (2020) 105821, <https://doi.org/10.1016/j.porgcoat.2020.105821>.
- R. Auvergne, S. Caillol, G. David, B. Boutevin, J.-P. Pascault, Biobased thermosetting epoxy: present and future, *Chem. Rev.* 114 (2014) 1082–1115, <https://doi.org/10.1021/cr3001274>.
- S.I. Bhat, M. Mobin, S. Islam, S. Zehra, Shahid-ul-Islam, Recent advances in anticorrosive coatings based on sustainable polymers: challenges and perspectives, *Surf. Coat. Technol.* 480 (2024) 130596, <https://doi.org/10.1016/j.surfcoat.2024.130596>.
- C. Noè, L. Iannucci, S. Malburet, A. Graillot, M. Sangermano, S. Grassini, New UV-curable anticorrosion coatings from vegetable oils, *Macromol. Mater. Eng.* 306 (2021), <https://doi.org/10.1002/mame.202100029>.
- S. Miao, P. Wang, Z. Su, S. Zhang, Vegetable-oil-based polymers as future polymeric biomaterials, *Acta Biomater.* 10 (2014) 1692–1704, <https://doi.org/10.1016/j.actbio.2013.08.040>.
- R. Sesia, A.G. Cardone, S. Ferraris, S. Spriano, M. Sangermano, Exploitation of tannic acid as additive for the adhesion enhancement of UV-curable bio-based coating, *Prog. Org. Coating* 189 (2024) 108311, <https://doi.org/10.1016/j.porgcoat.2024.108311>.
- J. Ramezanzadeh, B. Ramezanzadeh, N.A. Samani, Progress in bio-based anti-corrosion coatings; A concise overview of the advancements, constraints, and advantages, *Prog. Org. Coating* 194 (2024) 108556, <https://doi.org/10.1016/j.porgcoat.2024.108556>.
- L. Pezzana, G. Melilli, P. Delliere, D. Moraru, N. Guigo, N. Sbirrazzuoli, M. Sangermano, Thiol-ene biobased networks: furan allyl derivatives for green coating applications, *Prog. Org. Coating* 173 (2022) 107203, <https://doi.org/10.1016/j.porgcoat.2022.107203>.
- A. Truncale, T. Laxminarayan, N. Rajagopalan, C.E. Weinell, S. Kil, M. Johansson, Epoxidized technical Kraft lignin as a particulate resin component for high-performance anticorrosive coatings, *J. Coating Technol. Res.* (2024), <https://doi.org/10.1007/s11998-023-00899-9>.
- M. Faccini, L. Bautista, L. Soldi, A.M. Escobar, M. Altavilla, M. Calvet, A. Doménech, E. Domínguez, Environmentally friendly anticorrosive polymeric coatings, *Appl. Sci.* 11 (2021) 3446, <https://doi.org/10.3390/app11083446>.
- S. Spriano, A. Dmitruk, K. Naplocha, S. Ferraris, Tannic acid coatings to control the degradation of AZ91 Mg alloy porous structures, *Metals* 13 (2023) 200, <https://doi.org/10.3390/met13020200>.
- H. Okumura, Application of phenolic compounds in plants for green chemical materials, *Curr. Opin. Green Sustainable Chem.* 27 (2021) 100418, <https://doi.org/10.1016/j.cogsc.2020.100418>.
- A.K. Das, MdN. Islam, MdO. Faruk, Md Ashaduzzaman, R. Dungani, Review on tannins: extraction processes, applications and possibilities, *South Afr. J. Bot.* 135 (2020) 58–70, <https://doi.org/10.1016/j.sajb.2020.08.008>.
- S. Sharma, R. Ganjoo, A. Kumar, Polyphenols for anticorrosion application, in: *Science and Engineering of Polyphenols*, Wiley, 2024, pp. 134–156, <https://doi.org/10.1002/9781394203932.ch6>.
- L.Q. Xu, D. Pranantyo, K.-G. Neoh, E.-T. Kang, G.D. Fu, Thiol reactive maleimido-containing tannic acid for the bioinspired surface anchoring and post-functionalization of antifouling coatings, *ACS Sustain. Chem. Eng.* 4 (2016) 4264–4272, <https://doi.org/10.1021/acssuschemeng.6b00760>.
- X. Wang, J. Zhang, J. Liu, R. Liu, J. Luo, Synthesis of acrylated tannic acid as bio-based adhesion promoter in UV-curable coating with improved corrosion resistance, *Colloids Surf. A Physicochem. Eng. Asp.* 644 (2022), <https://doi.org/10.1016/j.colsurfa.2022.128834>.
- R. Ding, Y. Du, R.B. Goncalves, L.F. Francis, T.M. Reineke, Sustainable near UV-curable acrylates based on natural phenolics for stereolithography 3D printing, *Polym. Chem.* 10 (2019) 1067–1077, <https://doi.org/10.1039/c8py01652f>.
- A. Liguori, S. Subramanian, J.G. Yao, M. Hakkarainen, Photocurable extended vanillin-based resin for mechanically and chemically recyclable, self-healable and digital light processing 3D printable thermosets, *Eur. Polym. J.* 178 (2022), <https://doi.org/10.1016/j.eurpolymj.2022.111489>.
- E. Shin, J. Yoo, G. Yoo, Y.J. Kim, Y.S. Kim, Eco-friendly cross-linked polymeric dielectric material based on natural tannic acid, *Chem. Eng. J.* 358 (2019) 170–175, <https://doi.org/10.1016/j.cej.2018.09.176>.
- J. Fouilloux, S. Abbad Andaloussi, V. Langlois, L. Dammak, E. Renard, Chemical modification of commercial fabrics by photoinduced grafting tannic acid to produce antioxidant and antibacterial textiles, *Sustainability* 16 (2024), <https://doi.org/10.3390/su16114352>.
- W. Thielemans, R.P. Wool, Lignin esters for use in unsaturated thermosets: lignin modification and solubility modeling, *Biomacromolecules* 6 (2005) 1895–1905, <https://doi.org/10.1021/bm0500345>.
- K. Martina, G. Cravotto, R.S. Varma, Impact of microwaves on organic synthesis and strategies toward flow processes and scaling up, *J. Org. Chem.* 86 (2021) 13857–13872, <https://doi.org/10.1021/acs.joc.1c00865>.
- J. Yao, K. Odelius, M. Hakkarainen, Microwave hydrophobized lignin with antioxidant activity for fused filament fabrication, *ACS Appl. Polym. Mater.* 3 (2021) 3538–3548, <https://doi.org/10.1021/acsapm.1c00438>.
- J. Yao, M. Karlsson, M. Lawoko, K. Odelius, M. Hakkarainen, Microwave-assisted organosolv extraction for more native-like lignin and its application as a property-enhancing filler in a light processable biobased resin, *RSC Sustainability* 1 (2023) 1211–1222, <https://doi.org/10.1039/D3SU00115F>.
- A. Truncale, I. Ribca, J. Yao, M. Hakkarainen, M. Johansson, <sc>fractionation and functionalization of technical lignin toward thermoset resins, *J. Appl. Polym. Sci.* 140 (2023), <https://doi.org/10.1002/app.54645>.
- R. Sesia, M. Porcarello, M. Hakkarainen, S. Ferraris, S. Spriano, M. Sangermano, Sustainable light-assisted 3D printing of bio-based microwave-functionalized gallic acid, *Macromol. Chem. Phys.* (2024), <https://doi.org/10.1002/macp.202400181>.

- [40] L. Pezzana, M. Sangermano, Fully biobased UV-cured thiol-ene coatings, *Prog. Org. Coating* 157 (2021) 106295, <https://doi.org/10.1016/j.porgcoat.2021.106295>.
- [41] S. Pradheebha, R. Unnikannan, R.N. Bathe, G. Padmanabham, R. Subasri, Effect of plasma pretreatment on durability of sol-gel superhydrophobic coatings on laser modified stainless steel substrates, *J. Adhes. Sci. Technol.* 32 (2018) 2394–2404, <https://doi.org/10.1080/01694243.2018.1482735>.
- [42] Y. Sun, T. Bell, Plasma surface engineering of low alloy steel, *Mater. Sci. Eng.* 140 (1991) 419–434, [https://doi.org/10.1016/0921-5093\(91\)90458-Y](https://doi.org/10.1016/0921-5093(91)90458-Y).
- [43] ASTM International, Standard specification for steel, sheet, cold-rolled, carbon, structural, high-strength low-alloy, high-strength low-alloy with improved formability, required hardness, solution hardened, and, Bake Hardenable. ASTM A1008/A1008M-24 Standard (2024), https://doi.org/10.1520/A1008_A1008M-24.
- [44] J. Yao, M. Hakkarainen, Methacrylated wood flour-reinforced “all-wood” derived resin for digital light processing (DLP) 3D printing, *Compos. Commun.* 38 (2023), <https://doi.org/10.1016/j.coco.2023.101506>.
- [45] X. Meng, C. Crestini, H. Ben, N. Hao, Y. Pu, A.J. Ragauskas, D.S. Argyropoulos, Determination of hydroxyl groups in biorefinery resources via quantitative ³¹P NMR spectroscopy, *Nat. Protoc.* 14 (2019) 2627–2647, <https://doi.org/10.1038/s41596-019-0191-1>.
- [46] F. Melone, R. Saladino, H. Lange, C. Crestini, Tannin structural elucidation and quantitative ³¹P NMR analysis. 2. Hydrolyzable tannins and proanthocyanidins, *J. Agric. Food Chem.* 61 (2013) 9316–9324, <https://doi.org/10.1021/jf401664a>.
- [47] R. Sesia, S. Ferraris, M. Sangermano, S. Spriano, UV-cured chitosan-based hydrogels strengthened by tannic acid for the removal of copper ions from water, *Polymers* 14 (2022) 4645, <https://doi.org/10.3390/polym14214645>.
- [48] L. Ford, K. Theodoridou, G.N. Sheldrake, P.J. Walsh, A critical review of analytical methods used for the chemical characterisation and quantification of phlorotannin compounds in brown seaweeds, *Phytochem. Anal.* 30 (2019) 587–599, <https://doi.org/10.1002/pca.2851>.
- [49] A. Cosola, A. Chiappone, M. Sangermano, Changing the surface properties with a “click”: functionalization of DLP-printed structures exploiting residual acrylate functions, *Mon Syst Des Eng* 7 (2022) 1093–1101, <https://doi.org/10.1039/D2ME00059H>.
- [50] M. Bergoglio, Z. Najmi, A. Cochis, M. Miola, E. Vernè, M. Sangermano, UV-cured bio-based acrylated soybean oil scaffold reinforced with bioactive glasses, *Polymers* 15 (2023) 4089, <https://doi.org/10.3390/polym15204089>.
- [51] M. Porcarello, S. Bonardd, G. Kortaberria, Y. Miyaji, K. Matsukawa, M. Sangermano, 3D printing of electrically conductive objects with biobased polyglycerol acrylic monomers, *ACS Appl. Polym. Mater.* 6 (2024) 2868–2876, <https://doi.org/10.1021/acsapm.3c03073>.
- [52] M. Rahimnejad, T. Labonté-Dupuis, N.R. Demarquette, S. Lerouge, A rheological approach to assess the printability of thermosensitive chitosan-based biomaterial inks, *Biomed. Mater.* 16 (2021) 015003, <https://doi.org/10.1088/1748-605X/abb2d8>.
- [53] M. Zanon, A. Chiappone, N. Garino, M. Canta, F. Frascella, M. Hakkarainen, C. F. Pirri, M. Sangermano, Microwave-assisted methacrylation of chitosan for 3D printable hydrogels in tissue engineering, *Mater Adv* 3 (2022) 514–525, <https://doi.org/10.1039/D1MA00765C>.
- [54] ASTM International, Standard Test Method for Leeb Hardness Testing of Steel Products, ASTM A956/A956M, 2022, https://doi.org/10.1520/A0956_A0956M-17A.
- [55] ASTM International, Standard Test Method for Rubber Property—Durometer Hardness, D2vols. 240–15, ASTM, 2021, <https://doi.org/10.1520/D2240-15R21>.
- [56] A. Pizzi, Tannins: prospectives and actual industrial applications, *Biomolecules* 9 (2019), <https://doi.org/10.3390/biom9080344>.
- [57] G. Zhu, J. Zhang, J. Huang, X. Yu, J. Cheng, Q. Shang, Y. Hu, C. Liu, L. Hu, Y. Zhou, High-performance 3D printing UV-curable resins derived from soybean oil and gallic acid, *Green Chem.* 23 (2021) 5911–5923, <https://doi.org/10.1039/d1gc01934a>.
- [58] A. Khalil, C. Gerardin-Charbonnier, H. Chapuis, K. Ferji, J.-L. Six, Original bio-based antioxidant poly(meth)acrylate from gallic acid-based monomers, *ACS Sustain. Chem. Eng.* 9 (2021) 11458–11468, <https://doi.org/10.1021/acssuschemeng.1c03607>.
- [59] N.S. Sangaj, V.C. Malshe, Permeability of polymers in protective organic coatings, *Prog. Org. Coating* 50 (2004) 28–39, <https://doi.org/10.1016/j.porgcoat.2003.09.015>.
- [60] A.J. Hill, A.W. Thornton, R.H.J. Hannink, J.D. Moon, B.D. Freeman, Role of free volume in molecular mobility and performance of glassy polymers for corrosion-protective coatings, *Corrosion Engineering, Sci. Technol.* 55 (2020) 145–158, <https://doi.org/10.1080/1478422X.2019.1701237>.
- [61] C. Zhang, S.A. Madbouly, M.R. Kessler, Renewable polymers prepared from vanillin and its derivatives, *Macromol. Chem. Phys.* 216 (2015) 1816–1822, <https://doi.org/10.1002/macp.201500194>.
- [62] J.F. Stanzione III, J.M. Sadler, J.J. La Scala, K.H. Reno, R.P. Wool, Vanillin-based resin for use in composite applications, *Green Chem.* 14 (2012) 2346, <https://doi.org/10.1039/c2gc35672d>.
- [63] D. Liang, Y. Zhou, X. Liu, Q. Zhou, B. Huang, E. Zhang, Q. Chen, J. Shen, Wettability and corrosion performance of arc-sprayed Fe-based amorphous coatings, *Surf. Coat. Technol.* 433 (2022) 128129, <https://doi.org/10.1016/j.surfcoat.2022.128129>.
- [64] L. Iannucci, J.F. Ríos-Rojas, E. Angelini, M. Parvis, S. Grassini, Electrochemical characterization of innovative hybrid coatings for metallic artefacts, *The European Physical Journal Plus* 133 (2018) 522, <https://doi.org/10.1140/epjp/i2018-12368-3>.
- [65] M. Calovi, S. Rossi, Functional olive pit powders: the role of the bio-based filler in reducing the water uptake phenomena of the waterborne paint, *Coatings* 13 (2023) 442, <https://doi.org/10.3390/coatings13020442>.
- [66] S. Rossi, F. Russo, M. Calovi, M. del Rincón, D. Velez, The influence of the size of corundum particles on the properties of chemically resistant porcelain enamels, *Ceram. Int.* 47 (2021) 11618–11627, <https://doi.org/10.1016/j.ceramint.2021.01.001>.
- [67] S. Rossi, M. Calovi, D. Velez, J. Munoz, Influence of addition of hard particles on the mechanical and chemical behavior of vitreous enamel, *Surf. Coat. Technol.* 357 (2019) 69–77, <https://doi.org/10.1016/j.surfcoat.2018.09.062>.
- [68] M. Periolatto, M. Sangermano, P.R. Spena, Photocured epoxy/graphene nanocomposites with enhanced water vapor barrier properties, <https://doi.org/10.1063/1.4949619>, 2016.
- [69] L. Calabrese, A. Khaskoussi, E. Proverbio, Wettability and anti-corrosion performances of carbon nanotube-silane composite coatings, *Fibers* 8 (2020) 57, <https://doi.org/10.3390/fib8090057>.
- [70] S. Lee, Y. Lai, T. Hsu, Influence of polymerization conditions on monomer elution and microhardness of autopolymerized polymethyl methacrylate resin, *Eur. J. Oral Sci.* 110 (2002) 179–183, <https://doi.org/10.1034/j.1600-0722.2002.11232.x>.
- [71] F.J. Rojas-Macedo, B. Teutle-Coyotecatl, R. Contreras-Bulnes, L.E. Rodríguez-Vilchis, E. Reyes-Cervantes, U. Velazquez-Enriquez, Effect of polymerization methods on surface roughness and hardness of commercially available self-curing acrylic resins: a comparative study, *Pigment Resin Technol.* (2024), <https://doi.org/10.1108/PRT-12-2023-0120>.
- [72] D. Wei, X. Huang, J. Zeng, S. Deng, J. Xu, Facile synthesis of a castor oil-based hyperbranched acrylate oligomer and its application in UV-curable coatings, *J. Appl. Polym. Sci.* 137 (2020), <https://doi.org/10.1002/app.49054>.
- [73] I.O. Arukalam, I.O. Madu, E.Y. Ishidi, High performance characteristics of Lupinus arboreus gum extract as self-healing and corrosion inhibition agent in epoxy-based coating, *Prog. Org. Coating* 151 (2021) 106095, <https://doi.org/10.1016/j.porgcoat.2020.106095>.
- [74] K. Thiele, N. Eversmann, A. Krombholz, D. Pufky-Heinrich, Bio-based epoxy resins based on linseed oil cured with naturally occurring acids, *Polymers* 11 (2019) 1409, <https://doi.org/10.3390/polym11091409>.
- [75] L. Pezzana, A. Emanuele, R. Sesana, C. Delprete, E. Malmström, M. Johansson, M. Sangermano, Cationic UV-curing of isosorbide-based epoxy coating reinforced with macadamia nut shell powder, *Prog. Org. Coating* 185 (2023) 107949, <https://doi.org/10.1016/j.porgcoat.2023.107949>.
- [76] K. Wei, Y. Qu, J. Li, L. Chen, J. Du, W. Xue, Surface charge and corrosion behavior of plasma electrolytic oxidation film on Zr3Al based alloy, *Surf. Coat. Technol.* 357 (2019) 412–417, <https://doi.org/10.1016/j.surfcoat.2018.10.036>.
- [77] K. Wei, L. Chen, Y. Qu, Y. Zhang, X. Jin, W. Xue, J. Zhang, Zeta potential of microarc oxidation film on zirconium alloy in different aqueous solutions, *Corrosion Sci.* 143 (2018) 129–135, <https://doi.org/10.1016/j.corsci.2018.08.006>.
- [78] M. Kendig, S. Jeanjaquet, R. Addison, J. Waldrop, Role of hexavalent chromium in the inhibition of corrosion of aluminum alloys, *Surf. Coat. Technol.* 140 (2001) 58–66, [https://doi.org/10.1016/S0257-8972\(01\)01099-4](https://doi.org/10.1016/S0257-8972(01)01099-4).
- [79] Z. Zhai, L. Feng, Effect of oxygen plasma treatment on bonding strength of epoxy coating on steel substrate, *Prog. Org. Coating* 131 (2019) 36–41, <https://doi.org/10.1016/j.porgcoat.2019.02.011>.
- [80] S. Ferraris, M. Prato, C. Veneis, A. Varesano, G. Gautier di Configno, S. Spriano, Coupling of keratin with titanium: a physico-chemical characterization of functionalized or coated surfaces, *Surf. Coat. Technol.* 397 (2020) 126057, <https://doi.org/10.1016/j.surfcoat.2020.126057>.
- [81] A. Anderez, F.J. Alguacil, F.A. López, Acid pickling of carbon steel, *Rev. Metal. (Madr.)* 58 (2022) e226, <https://doi.org/10.3989/revmetalm.226>.
- [82] M. Calovi, V. Coroneo, S. Palanti, S. Rossi, Colloidal silver as innovative multifunctional pigment: the effect of Ag concentration on the durability and biocidal activity of wood paints, *Prog. Org. Coating* 175 (2023) 107354, <https://doi.org/10.1016/j.porgcoat.2022.107354>.
- [83] F. Deflorian, S. Rossi, An EIS study of ion diffusion through organic coatings, *Electrochim. Acta* 51 (2006) 1736–1744, <https://doi.org/10.1016/j.electacta.2005.02.145>.
- [84] E. Akbarinezhad, M. Bahremandi, H.R. Faridi, F. Rezaei, Another approach for ranking and evaluating organic paint coatings via electrochemical impedance spectroscopy, *Corrosion Sci.* 51 (2009) 356–363, <https://doi.org/10.1016/j.corsci.2008.10.029>.
- [85] E. Scrinzi, S. Rossi, F. Deflorian, Effect of slurry mechanical damage on the properties of an organic coating system, *Surf. Coat. Technol.* 203 (2009) 2974–2981, <https://doi.org/10.1016/j.surfcoat.2009.03.025>.
- [86] A. Amirudin, D. Thieny, Application of electrochemical impedance spectroscopy to study the degradation of polymer-coated metals, *Prog. Org. Coating* 26 (1995) 1–28, [https://doi.org/10.1016/0300-9440\(95\)00581-1](https://doi.org/10.1016/0300-9440(95)00581-1).
- [87] I.C.P. Margarit-Mattos, EIS and organic coatings performance: revisiting some key points, *Electrochim. Acta* 354 (2020) 136725, <https://doi.org/10.1016/j.electacta.2020.136725>.
- [88] E. Barsoukov, J.R. Macdonald (Eds.), *Impedance Spectroscopy*, Wiley, 2018, <https://doi.org/10.1002/9781119381860>.
- [89] H. Hlushko, Y. Cubides, R. Hlushko, T.M. Kelly, H. Castaneda, S.A. Sukhishvili, Hydrophobic antioxidant polymers for corrosion protection of an aluminum alloy, *ACS Sustain. Chem. Eng.* 6 (2018) 14302–14313, <https://doi.org/10.1021/acssuschemeng.8b02966>.
- [90] R. Sesia, S. Spriano, M. Sangermano, M. Calovi, S. Rossi, S. Ferraris, Natural tannin layers for the corrosion protection of steel in contact with water-based media, *Coatings* 14 (2024) 965, <https://doi.org/10.3390/coatings14080965>.